ADVANCED MATERIALS

Supporting Information

for *Adv. Mater.*, DOI: 10.1002/adma.201701044

Millivolt Modulation of Plasmonic Metasurface Optical Response via Ionic Conductance

*Krishnan Thyagarajan, Ruzan Sokhoyan, Leonardo Zornberg, and Harry A. Atwater**

Supporting Information

Article type: Communication

Millivolt Modulation of Plasmonic Metasurface Optical Response via Ionic Conductance

Krishnan Thyagarajan, Ruzan Sokhoyan, Leonardo Zornberg, and Harry A. Atwater[*]

Dr. K. Thyagarajan, Dr. R. Sokhoyan, L. Zornberg, Prof. H. A. Atwater

Thomas J. Watson Laboratory of Applied Physics,

California Institute of Technology,

Pasadena, California 91125, USA

E-mail: haa@caltech.edu

Dr. K. Thyagarajan, Prof. H. A. Atwater

Kavli Nanoscience Institute,

California Institute of Technology,

Pasadena, California 91125, USA

Keywords: Tunable metasurface, filament formation, ionic transport, memristor, indium tin oxide (ITO)

S1. Comparative analysis of previously reported tunable metasurfaces

In what follows we review the details of previously reported active metasurfaces and explain challenges associated with obtaining tunable optical response in the visible wavelength range.

Field effect in semiconductors

In this scheme, each metasurface element is effectively a metal-insulator-semiconductor (MIS) capacitor with the metal serving as a gate and the semiconductor functioning as a field effect channel[1]. When an electrical bias is applied between metal gate and semiconductor, a charge depletion or accumulation layer is formed in the semiconductor at the interface of the semiconductor and insulator. This results in modulation of the semiconductor dielectric permittivity, altering the optical response of a metasurface.

From ellipsometry measurements it is known that the dielectric permittivity of doped semiconductors can be typically described by a Drude-Lorentz model which is sum of a Drude term and Lorentz oscillators. It is typically assumed that the Lorentz oscillators do not depend on field or voltage. On the other hand, the Drude term reads $\varepsilon = \varepsilon_\infty - \omega^2_p/(\omega^2 + i\omega\Gamma)$ where ω_p is the plasma frequency which is related to the carrier density N and electron effective mass m^* as $\omega_p^2 = Ne^2/(\varepsilon_0 m^*)$. Here ε_0 is the dielectric permittivity of vacuum, e is the electron charge, and Γ is the damping constant. Thus, the Drude term increases linearly with carrier concentration. For a given change of semiconductor carrier density, the variation of the complex dielectric permittivity will be higher at lower frequencies, or, equivalently, at longer wavelengths. This constitutes one of the reasons why field effect modulation of the optical response of a metasurface is challenging in the visible wavelength range.

When studying tunable metasurfaces with GaAs or indium tin oxide (ITO) field-effect channels, it has been shown that the epsilon-near-zero (ENZ) transition of a thin semiconductor accumulation or depletion layer yields large optical modulation. At the ENZ transition, the real part of the dielectric permittivity of a thin semiconductor layer changes its sign, undergoing a transition from an optically dielectric to an optically metallic phase. The wavelength at which the bias-induced ENZ transition may occur is primarily defined by the semiconductor carrier concentration. For example, the ENZ transition of GaAs with carrier concentration of 5.5×10^{18} cm^{-3} is in the mid-infrared wavelength range. On the other hand, the ENZ transition in the accumulation layer of ITO with a carrier concentration of 3×10^{20}

cm^{-3} occurs at a wavelength of 1.5 μm. In principle, one could incorporate into a metasurface a highly doped semiconductor such that ENZ wavelength of its accumulation layer lies in the visible. However to date, field-effect tunable metasurfaces have not been demonstrated in the visible.

One of the major advantages of this approach is its technological maturity. Indeed, contemporary low power integrated electronic circuit operation is based on field-effect dynamics in semiconductors. Another important advantage is high modulation frequency (or, equivalently, small response time). For example, for a device with area of 40×40 μm, a response time of 50 ns has been experimentally demonstrated.

A disadvantage of this approach is that complex refractive index of a semiconductor is varied only in an ultrathin layer. For example, for ITO with carrier concentration 3×10^{20} cm^{-3}, the thickness of the modulated layer is around 1 nm. This implies that to observe tunable optical response of a metasurface, one needs extreme light concentration in this ultrathin material layer which is typically achieved by using plasmonic structures. As a result, field effect tunable metasurfaces exhibit strong absorption in plasmonic materials and semiconductor.

Graphene gating

Tunable metasurfaces based on graphene gating have also been experimentally demonstrated[2, 3]. The dielectric permittivity of graphene is proportional to the square root of the carrier density in graphene and is inversely proportional to the frequency squared. As it is the case with field effect in semiconductors, here also modulation of dielectric permittivity of graphene is larger at longer wavelengths. So far graphene based gated metasurfaces have shown tunable response in the mid-infrared wavelength range. In principle, operation wavelength can be reduced by using high-k dielectrics to gate graphene. However, so far this has not been experimentally demonstrated.

Similar to the case of field effect in semiconductors, for observation of graphene based tunable metasurfaces one needs to concentrate optical field in a graphene sheet. This extreme field confinement in a graphene sheet is typically associated with increased optical losses. An important advantage of graphene metasurfaces is small response time. For example, response time <50 ns has been experimentally reported[3].

Reorientation of Liquid Crystal Molecules

Active tuning of optical response of metasurfaces loaded with liquid crystal molecules has been previously demonstrated in the near-infrared wavelength range[4]. One of the major drawbacks of liquid crystal loaded metasurfaces is anchoring of liquid crystal molecules to the surfaces of the structures. Since the thickness of liquid crystal layer affected by anchoring is comparable to the extension of the metasurface optical near fields, this will result in reduced modulation upon application of external stimuli. When the metasurface feature size is further reduced so that the operation wavelength of the metasurface is in the visible, adverse effects of liquid crystal anchoring become even more severe. We believe this is the major reason why liquid crystal loaded tunable metasurfaces have not been demonstrated in the visible. The advantage of this approach is broadband refractive index modulation, and 1 ms response time.

Phase change materials

A tunable optical response of a metasurface has also been demonstrated via refractive index modulation of vanadium dioxide (VO_2) upon heating[5]. Heating induces a metal-insulator transition in VO_2. This has been shown to significantly alter the optical response of the metasurface in the wavelength range from 1.5 μm to 5 μm[5]. Phase transition in GeSbTe (GST) has also been used to demonstrate a tunable metasurface in the near-infrared wavelength range $\lambda>1$ μm[6]. In this case the phase change in GST was induced either via heating the sample by placing it on a hot plate or via short high intensity laser pulses that locally raise the temperature of a phase change material. It is worth mentioning that refractive index modulation of VO_2 and GST is relatively modest in the visible wavelength range as compared to that in the near-infrared range. This is one of the reasons why tunable metasurfaces incorporating phase change materials show a tunable optical response in near-infrared wavelength range. Another reason is that operation in the visible implies small resonator sizes resulting in higher localization of optical fields. This local heating could interfere with phase change dynamics of GST or VO_2 thus hindering deterministic performance of the device.

S2. Reflectance from planar structures

We calculate reflectance of the planar stack shown in Figure S1a. In our calculations we use ellipsometrically measured dielectric permittivity of ITO, while for the dielectric permittivity of alumina we use tabulated Palik data[7]. First, we assume that the dielectric permittivity of silver can also be described by using tabulated Palik data[7]. In this case, for the considered wavelength range, calculated reflectance varies between 75% and 87%. However, measured reflectance is as low as 30% for wavelengths between 650 and 800 nm (see Figure 1). To identify the reason behind this discrepancy, we fabricated a control sample of 80 nm Ag on Si substrate and performed spectroscopic ellipsometry measurement every day for a week. Indeed, we observed temporal evolution of the dielectric permittivity of silver. Next, by using

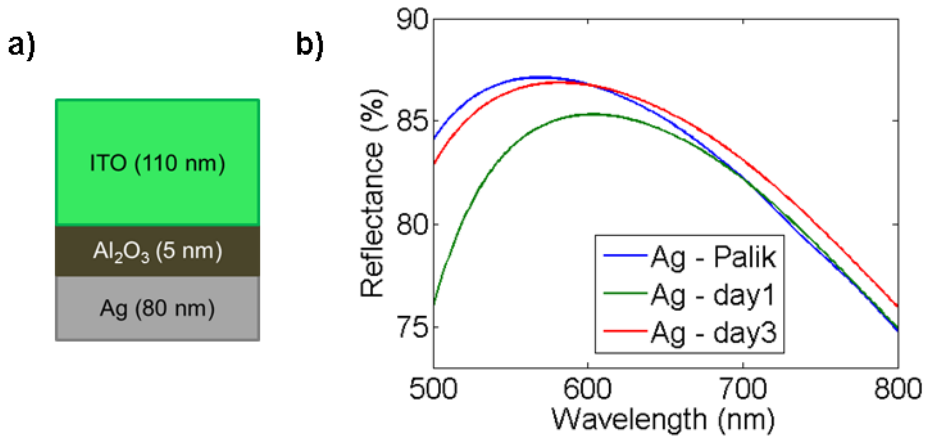

Figure S1. a) Schematic of the simulated structure; b) Calculated reflectance from the planar structure shown in (a). The legend indicates the dielectric permittivity used to model silver. In case of Ag – Palik the tabulated Palik data is used. Ag- day1 and Ag-day3 correspond to the ellipsometrically measured silver data 1 day and 3 days after deposition, correspondingly.

the reflectance from the structure (see Figure S1b). However, this variation is not substantial enough, to explain the discrepancy between theory and experiment.

spectroscopically measured dielectric permittivity values of silver, we calculated the reflectance from the planar heterostructure ($Ag/Al_2O_3/ITO$). We observe a minor variation of**S3. Transmission electron microscopy (TEM) images and energy-dispersive X-ray spectroscopy (EDS) of modulated films**

Transmission electron microscopy (TEM) images of the flat film configurations were made after the sample was exposed to repeated recycling at large voltages (2V).

A. Bare silicon substrate:

To compare the energy dispersive spectroscopy (EDS) signal across various regions of the sample, the bare silicon substrate was measured.

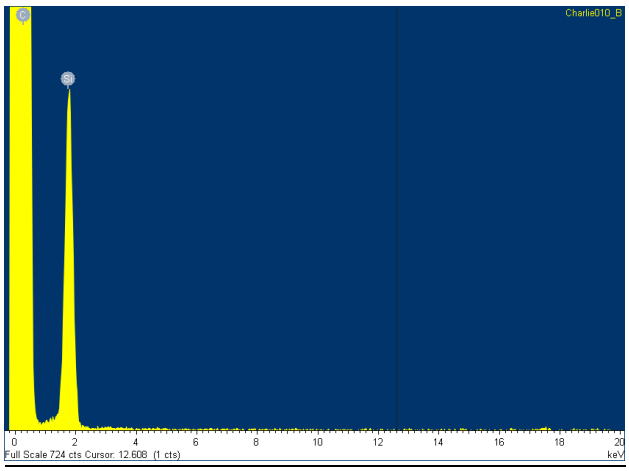

Figure S2A: EDS signal from bare silicon substrate showing a clear peak at around 1.8 keV

B. Indium tin oxide interface:

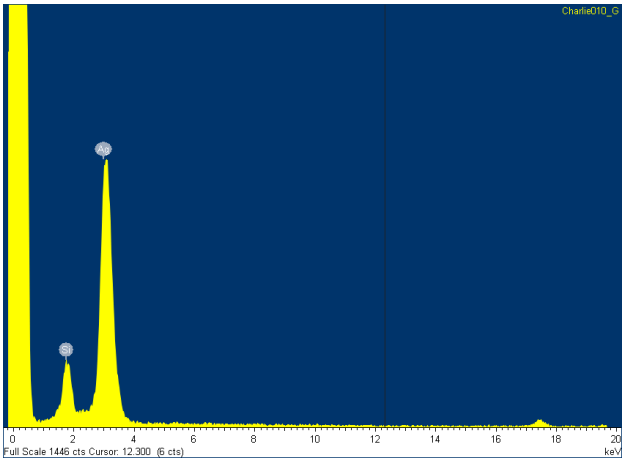

Figure S2B: EDS signal from the ITO layer. The molybdenum is from the TEM grid.

C. Silver and silicon interface:

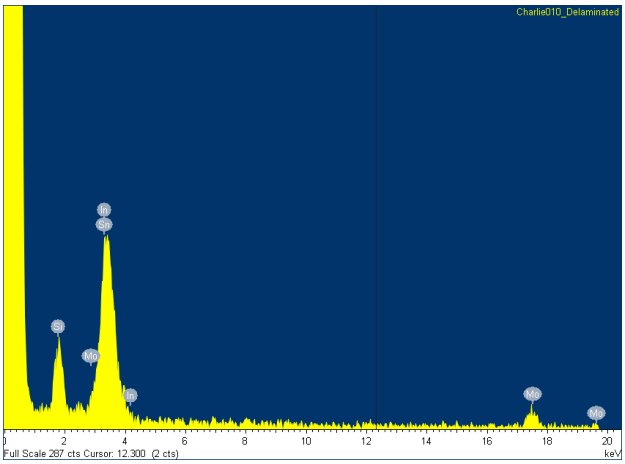

Figure S2C: The EDS signal from the interface of the silver and silicon clearly shows the presence of two elements. The small peak at higher energies is from the molybdenum present in the TEM sample grid.

D. Silver polycrystalline growth from the ITO alumina interface:

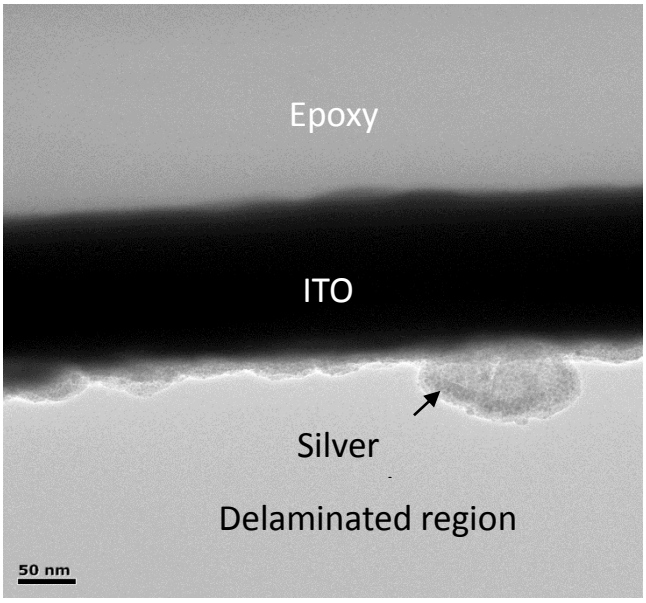

Figure S2D1: TEM image of the interface of the delaminated ITO surface showing the growth of the silver clusters from the interface downwards.

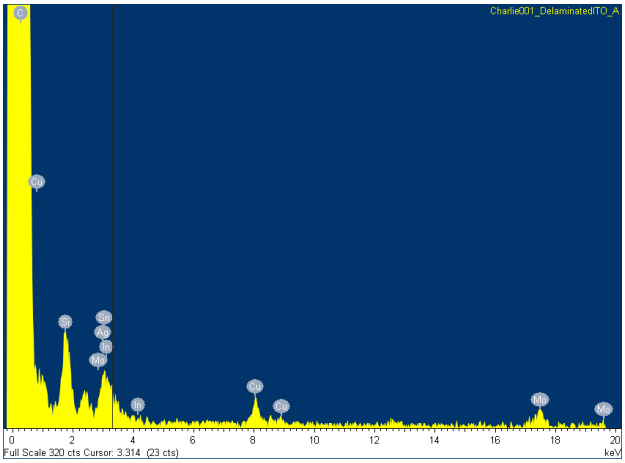

Figure S2D2: EDS analysis of the cluster and ITO interface shows the presence of indium, tin and silver in the region, indicating the existence of silver clusters.

S4. TEM images of Si/Cr/Ag/Al_2O_3/ITO planar heterostructure

We have performed an additional TEM analysis of Si/Cr/Ag/Al_2O_3/ITO planar heterostructure. This was done to ensure the smoothness/continuous nature of the very thin chromium layer. As shown below in the TEM images, the chromium layer is rather uniform with an average thickness of around 1.2 nm, compared to the expected 1 nm. The silver deposited using electron beam evaporation can clearly be seen to be polycrystalline.

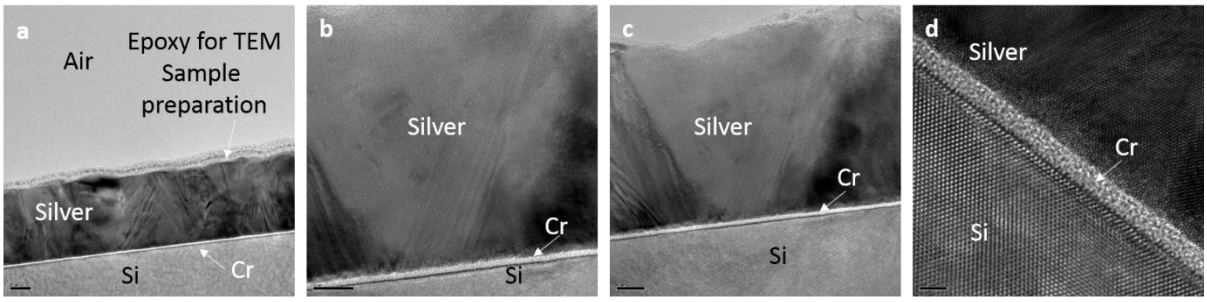

Figure S3. TEM images of Si/Cr/Ag/Al_2O_3/ITO planar heterostructure (a)-(d). The continuous layer of Cr can be seen across the sample. The scale bar in (d) corresponds to 1 nm. Evidently the silver appears to be polycrystalline.

S5. EDS of aged dolmen samples

We also undertook EDS analysis of planar structures discussed in Section S3. The presence of the expected elements was thus confirmed (Figure S4).

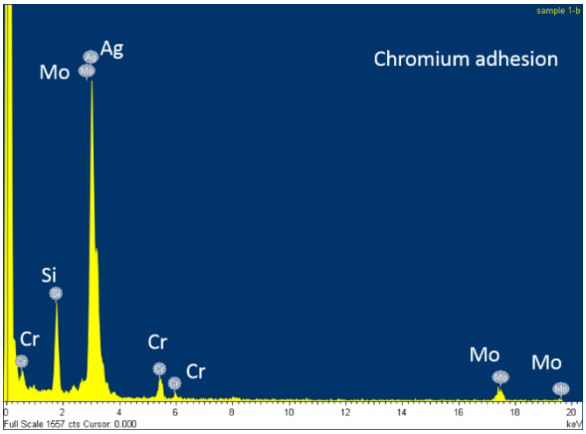

Figure S4. EDS measurements on the above mentioned samples clearly showed the presence of the expected elements. The molybdenum signal is from the TEM grids used during sample preparation.

S6. Energy dispersive spectroscopy maps of the dolmen structures

EDS was undertaken on the inverse dolmen samples with the chromium adhesion layer. Chemical maps derived from energy dispersive X-ray spectroscopy detailing the elements present in our samples were developed, and indicate the distribution of each element depicted by the color rendering. As can be clearly seen in Figure S5, there is sulphur and chlorine contamination in the samples.

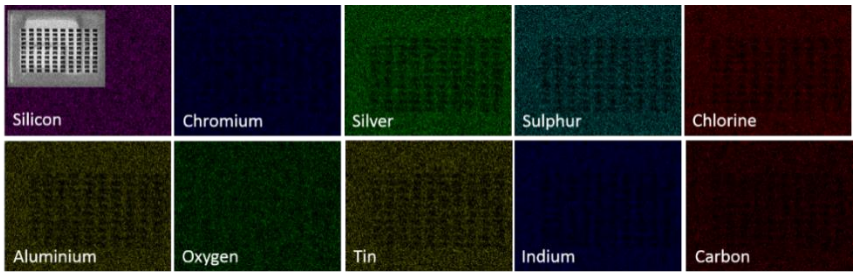

Figure S5. EDS undertaken on the inverse dolmen samples showed the presence of contaminants like sulphur and chlorine apart from the expected chemical elements. Their presence is hypothesized to improve the optical modulation with such a small applied bias.

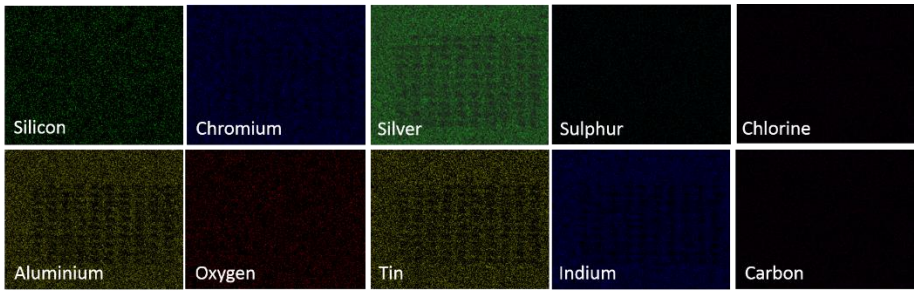

Figure S6. Energy dispersive X-ray spectroscopy undertaken on the fresh inverse dolmen samples did not show the presence of contaminants like sulphur and chlorine. These measurements were taken immediately after the sample fabrication. Their absence helps explain why the absolute magnitude of modulation is greater for an aged sample.

S7. Simulating Reflectance and Transmittance of the Dolmen Metasurfaces

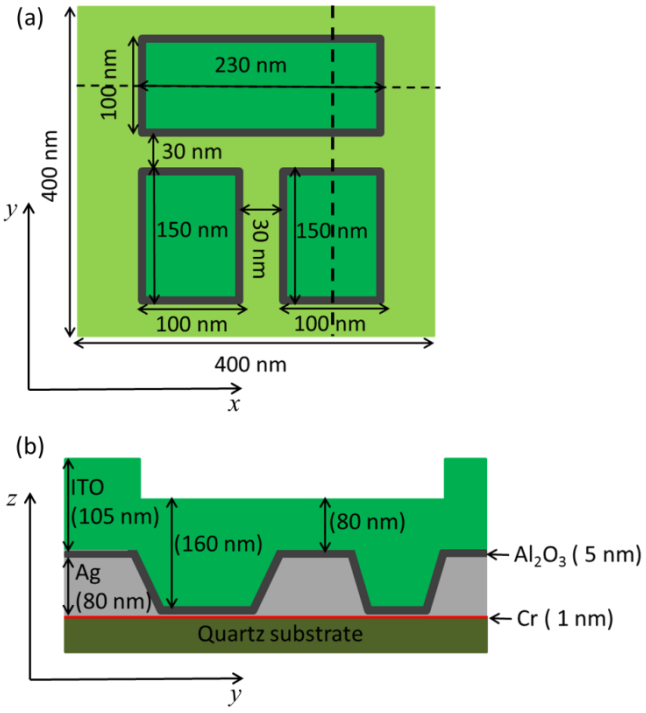

Figure S7. Schematic of the unit cell of the simulated dolmen metasurface. (a) Top view; (b) Cross-section of the metasurface. Cross-section is taken normally to the surface of the structure, along the dashed line shown in (a).

We use finite difference time domain (FDTD) method to simulate optical response of the metasurface. In our simulation we illuminate structure by plane wave and use periodic boundary conditions with period equal to 400 nm. Schematic of the top view of the simulated structure is shown in Figure S7 (a). The three rectangles indicate the dolmen structure which has been milled into silver via FIB. Dark grey frame of the rectangles is aimed to emphasize 5 nm thick alumina layer deposited via atomic layer deposition (even though alumina covers whole dolmen structure). The dimensions of the dolmen structures shown in Figure S7 (a) indicate the sizes of the rectangles milled in the silver film. This is schematically shown by extending arrows also over alumina layer. Figure S7 (b) shows vertical cross-section taken along the dashed line shown in Figure S7 (a). The considered cross-section is normal to the metasurface interface. As one can see from Figure S7 (b), the thickness of the silver film is 80 nm. In our simulation we took into account that each hole milled in the silver via FIB is not a rectangular parallel piped but rather a truncated pyramid with rectangular bases. Length of the top base of each truncated pyramid is 30 nm longer than length of the bottom base. Similarly, width of the top base of each truncated pyramid is 30 nm longer as compared to the width of the bottom base of each truncated pyramid. As one can see from Figures 3 (d), (f) and (h), the simulated reflectance and transmittance spectra match optical measurement results obtained from fresh dolmen samples under no applied bias. Finally, we note that silver was modelled by using tabulated Palik data, [7] while dielectric permittivity of ITO was obtained from ellipsometric measurement of 110 nm thick ITO film deposited on Si substrate.

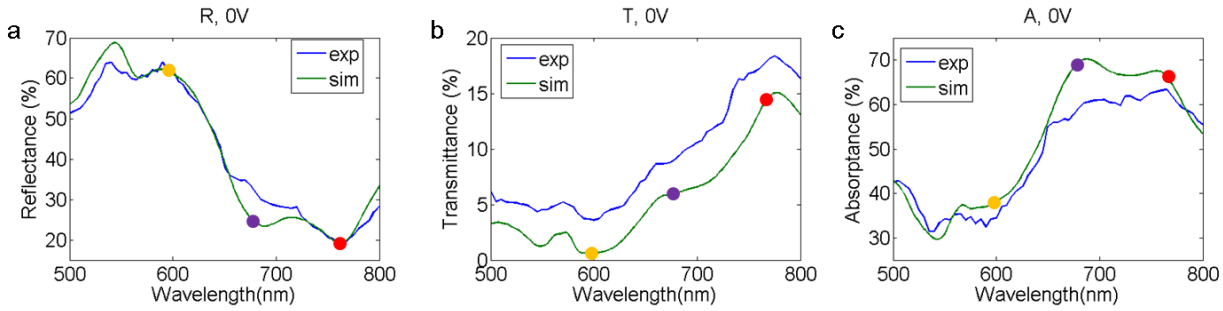

Figure S8: Simulated and measured reflectance, transmittance, and absorptance spectra of fresh dolmen metasurface. Yellow, purple, and red circles mark three wavelengths at which optical field profiles are displayed (see below).

Next we discuss spatial distribution of optical fields supported by a dolmen metasurface. We plot optical fields at three different wavelengths which are marked by yellow, purple, and red circles in Figure S8. Schematic of the top view of the simulated structure is shown in Figure S7 (a). Three rectangles indicate the dolmen structure which has been milled into silver via FIB. Dark grey frame of the rectangles is aimed to emphasize 5 nm thick alumina layer deposited via atomic layer deposition (even though alumina covers whole dolmen structure). The dimensions of the dolmen structures shown in Figure S7 (a) indicate the sizes of the rectangles milled in the silver film. This is schematically shown by extending arrows also over alumina layer. Figure S7 (b) shows vertical cross-section taken along the *vertical* dashed line shown in Figure S7 (a). The considered cross-section is normal to the metasurface interface.

Figure S9 shows spatial distribution of optical fields along the metasurface cross-section shown in Figure S7 (b). At $\lambda = 596$ nm and $\lambda = 760$ nm, we can see some hotspots on the top corners of the silver structures. One can see that although the hotspots are at similar locations and are of similar magnitudes at $\lambda = 596$ nm and $\lambda = 760$ nm, the latter demonstrates a larger volume over which the field is high (including the ITO region). We also see larger optical fields at the bottom of the structure at $\lambda = 760$ nm as compared to that at $\lambda = 596$ nm and $\lambda = 670$ nm. This could explain enhanced transmission observed at $\lambda = 760$ nm.

Next, we plot field profiles plotted (Figure S10) along the cross-section of the structure taken normally to the surface of the image, along the *horizontal* dashed line shown in Figure S7(a).

At λ= 596 nm, we observe significant electric field enhancement at Ag interface but there is no major *E*-field build up inside the structure. Note that at λ= 596 nm the reflectance of the incident plane wave is high. At λ=670 nm and λ = 760 nm, one can see a finite E-field build up in the ITO region of the structure, thus leading to larger losses due to the absorptive nature of ITO. It is also the region in which silver nucleation is taking place. Hence, a significant optical modulation is observed at wavelengths of λ=670 nm and λ = 760 nm. At λ = 760 nm the value of optical is higher at the bottom of dolmen structure. Since the field has now reached the bottom of dolmen structure, we observe relatively high transmission at λ = 760 nm as compared to the case of λ = 670 nm. Finally, other simulations done by us (not shown here) indicate that there is a finite coupling between optical fields supported by individual rods of a single inverse dolmen structure.

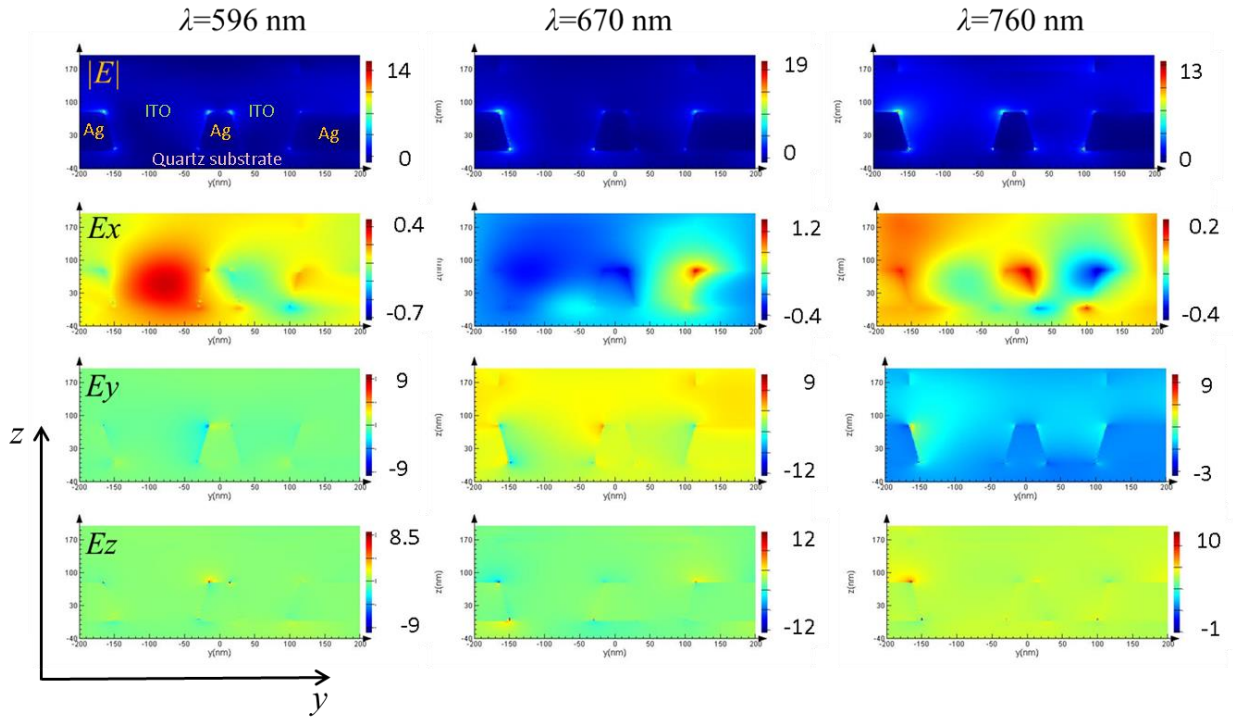

Figure S9: Field profiles plotted along the metasurface cross-section shown in Figure 3b.

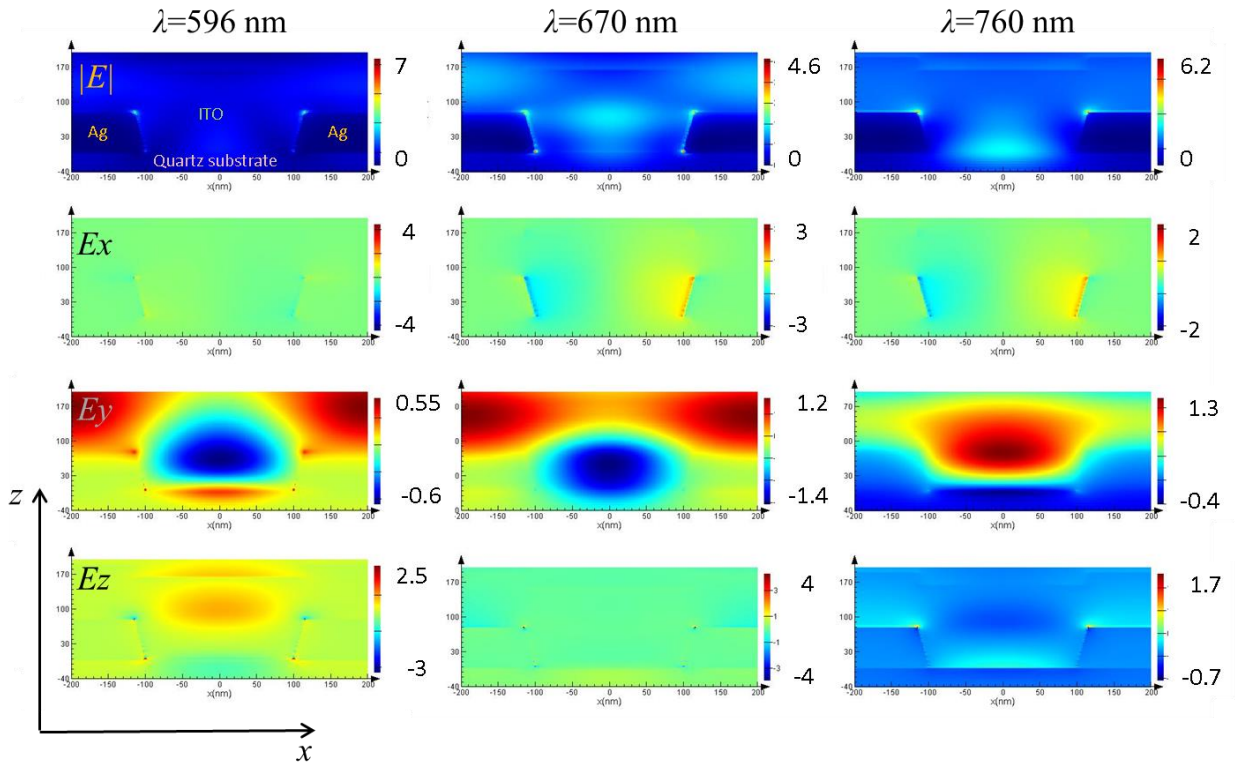

Figure S10. Field profiles plotted along the cross-section of the metasurface unit cell. The cross-section is taken normally to the surface of the structure, along the *horizontal* dashed line shown in Figure S7 (a).

S8. Reflectance from aged dolmen structures over larger voltage range

Figure S11 plots reflectance and transmittance from aged dolmen samples as a function of applied bias at wavelength of λ = 625 nm. For biases up to 6 mV, reflectance shows monotonic increase while transmittance shows monotonic decrease. Reflectance and transmittance spectra modulation in this bias range is shown in Figure 3 of the main manuscript. As one can see from Figure S11, upon increase of applied voltage beyond 6 mV, reflectance shows abrupt decrease, while transmittance shows abrupt increase. The data depicted in Figure S11 is an average over nine consecutive optical measurements performed on the device. The average absolute reflectance modulation upon application of 100 mV is 70.8% while the record absolute change of reflectance obtained from a single measurement is 78%.

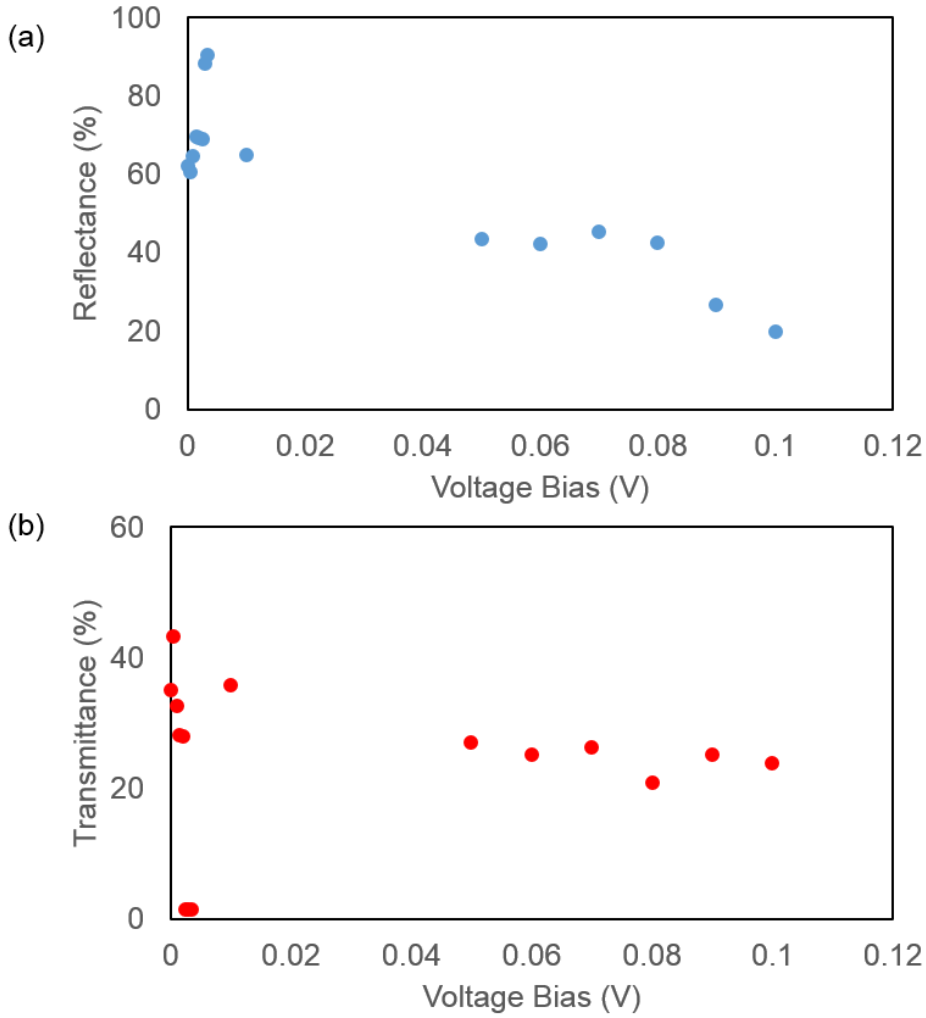

Figure S11. Measured (a) reflectance and (b) transmittance from the aged dolmen structures at λ = 625 nm, showing a modulation of up to 70.8 % in reflectance and 25.3 % in transmittance.

S9. Influence of continuity of the bottom electrode: Cr adhesion layer

We have also fabricated a set of inverse dolmen metasurface samples that do not contain thin metal film between bottom alumina and substrate. As it has been described in the main text of the manuscript, the inverse dolmen structure was written in 80 nm thin Ag film via FIB. To

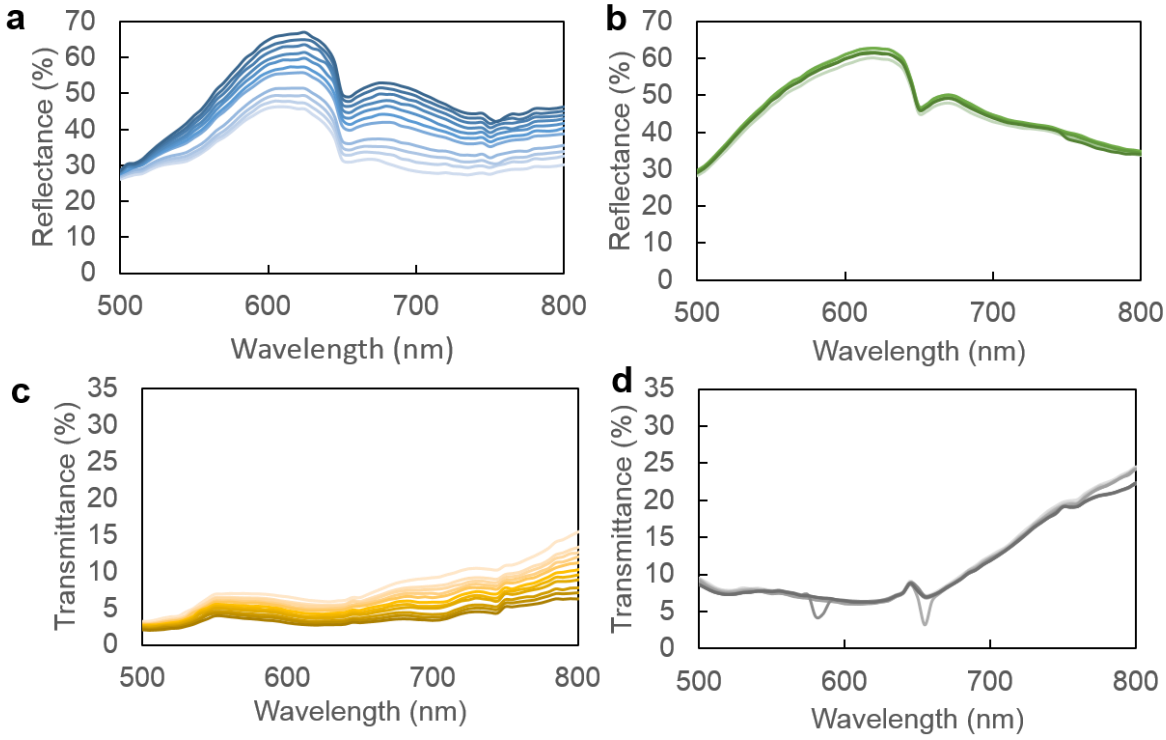

Figure S12. Measured reflectance (a) and (b) and transmittance (c) and (d) spectra with and without the chromium adhesion layer respectively showing the dramatic influence of the presence of chromium as an adhesion layer to permit the ultralow power millivolt level optical modulation.

obtain the samples without thin metal layer between bottom alumina and substrate, the FIB milling was interrupted only when whole bottom Ag and Cr layers were removed and substrate was reached. Interestingly, optical measurements performed on this set of samples showed negligible optical modulation (see Figure S12). Figures S12 (a) and S12 (c) show optical measurement results for samples with bottom electrode layer (also discussed in the main text of the manuscript) while Figures S12 (b) and S12 (d) indicate optical measurements performed on the samples that have been milled till reaching the substrate. The multiple curves show the measured reflectance when biasing silver positively with respect to ITO. The

light curve (0V) to dark curve (10 mV) is divided into 10 equal biases. Thus each curve represents an increase in 1 mV of applied bias. Interestingly, the samples which have been milled till substrate show negligible optical modulation (Figures S12 (b) and S12 (d)). The likely reason for this striking difference is that the bottom thin metal layer acts as an electrode that enables creation of electric field to push silver ions upwards, when electrical bias between silver and ITO is applied. To verify, that the difference between two sample sets is due to different electrostatic field distribution in the dolmen structure under applied bias, we fabricate additional set of inverse dolmen samples in which we use Ge adhesion layer instead of Cr.

S10. TEM images of planar Si/Ge/Ag planar samples:

First, we fabricate Si/Ge/Ag planar structures**.** Here Ge acts as an adhesion layer between Si and Ag. As can be seen from the TEM images (see Figure S13), the germanium layer is

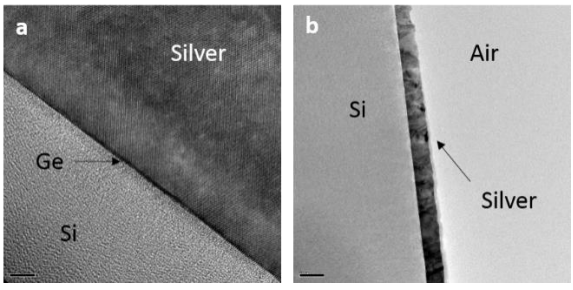

Figure S13. TEM images of Si/Ge/Ag heterostructure that contains 1 nm thick Ge adhesion layer (a), (b). The continuous layer of Ge can be clearly seen across the sample as pictured in (a).

rather uniform with an average thickness of around 1 nm. Again, as expected, the silver deposited using electron beam evaporation can clearly be seen to be polycrystalline.

S11. EDS of planar Si/Ge/Ag samples

EDS was performed on planar Si/Ge/Ag samples in order to ascertain the chemical composition of the deposited films. The presence of the expected elements was thus confirmed (Figure S14).

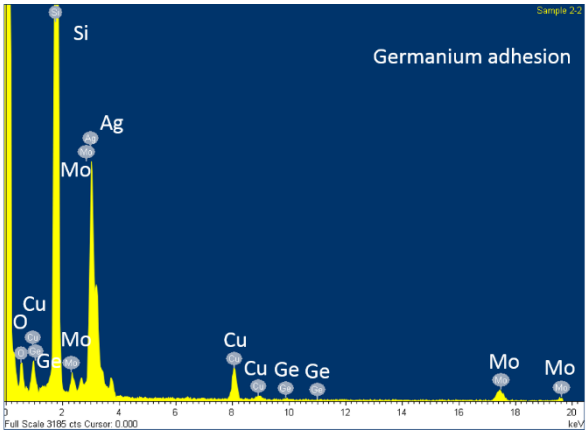

Figure S14. EDS measurements on the above mentioned samples clearly showed the presence of the expected elements. The molybdenum and copper signals are from the TEM grids used during sample preparation.

S12. Influence of continuity of the bottom electrode: germanium (Ge) adhesion layer

We have fabricated inverse dolmen structures using germanium as an adhesion layer instead of chromium. This was done in order to see if the observed modulation effect was particular to chromium or whether the modulation was observed even for the other conventional

adhesion layers used for such metal films. Optical reflection measurements were carried out on similar inverse dolmen structures using a germanium adhesion layer instead of a chromium layer. Unfortunately many of the samples showed some island formation in the germanium layer. Nevertheless, the modulation of the far-field optical reflection signal was clearly observed and the difference between the samples that contained thin metal layer between alumina and substrate and those that have been milled till the substrate was reached is discernable. The measurements are shown in Figure S15. The multiple curves show the measured reflection when applying an electrical bias between the ITO and silver/germanium. The light color (0V) to dark color (10 mV) is divided into 10 equal biases. Thus each curve represents an increase in 1 mV of applied bias, as shown in (a). The same ten curves are also plotted in (b) in the absence of thin metal layer between bottom alumina and substrate. Apparently these samples show no considerable optical modulation. Thus, enhanced optical modulation for samples containing thin metal layer between bottom alumina and the substrate is due to the presence of the dc electrical field pointing upward when ITO is negatively biased with respect to silver.

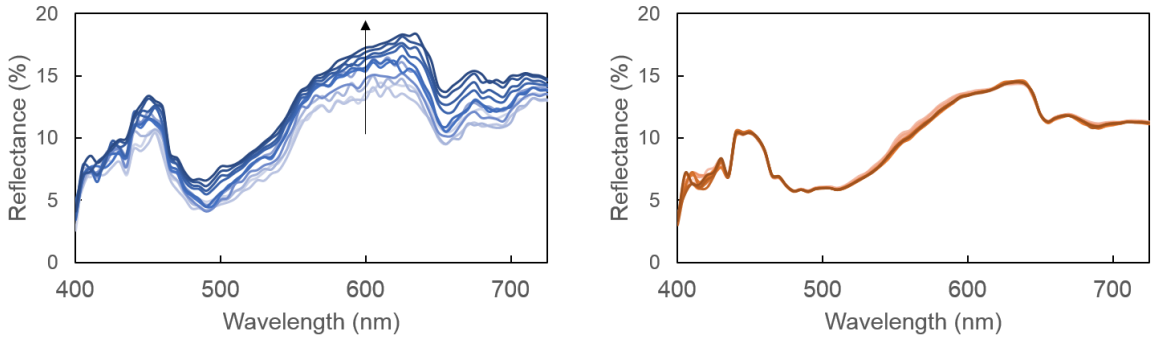

Figure S15. Experimentally measured optical far-field measurements from inverse dolmen structures when using germanium as an adhesion layer (left) and without an adhesion layer (right). The influence of an adhesion layer is again seen. Each blue curve in (a) represents an increase of 1 mV, starting from 0 mV to 10 mV.

S13. Cyclic voltammetry on aged dolmen samples

Cyclic voltammetry on the aged dolmen samples revealed a very small hysteresis loop over -8 mV to +8 mV as seen in Figure S16 (a). However, as is clear from Figure S16 (b) and (c), a significant hysteresis loop can be seen over a larger voltage range. This is a tell-tale sign of

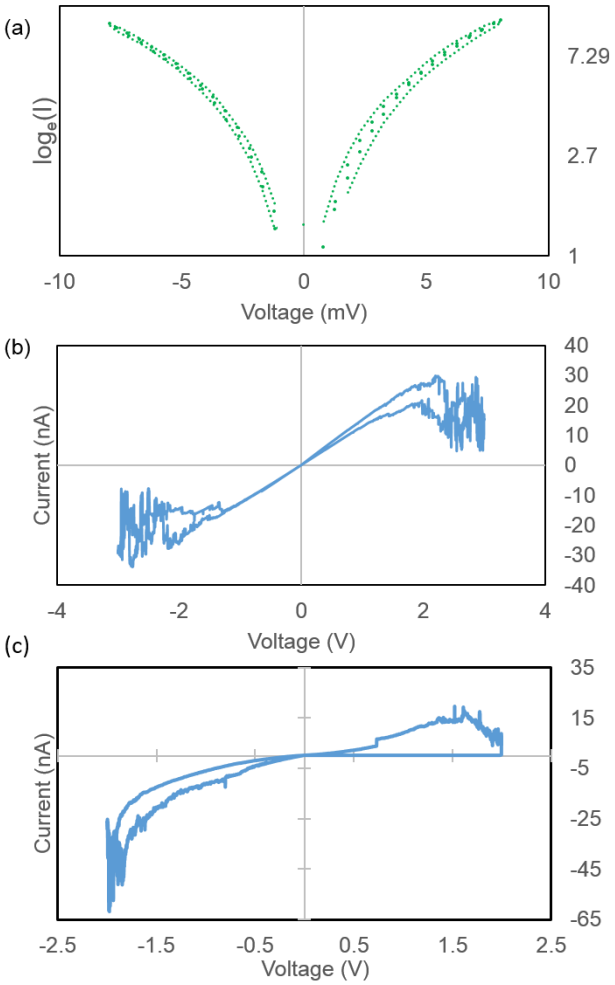

Figure S16. Experimentally measured cyclic voltammetry on the aged dolmen samples over a (a) smaller voltage range in millivolts and a (b) larger voltage range. In (a) we plot $\log_e$ of the current measured in nanoamps (nA). Large green dots are experimental points while small green dots indicate the moving squared average of the experimental points. A clear hysteresis sign can be seen in the latter figure providing hints towards a memristor type ionic conductance mechanism for the observed modulation.

the memristive like ionic conductance effect. When performing cyclic voltammetry measurements, we used the compliance current of 100 microamperes.

S14. Possibility to observe optical modulation over broad wavelength range

One of important **advantages** of our approach is that the observed optical modulation is inherently broadband. Optical modulation occurs due to nucleation and growth of silver nanoparticles in ITO. Since ITO and silver have very different values of complex dielectric permittivities in a broad wavelength range (Figure S17), one may expect a broadband optical modulation.

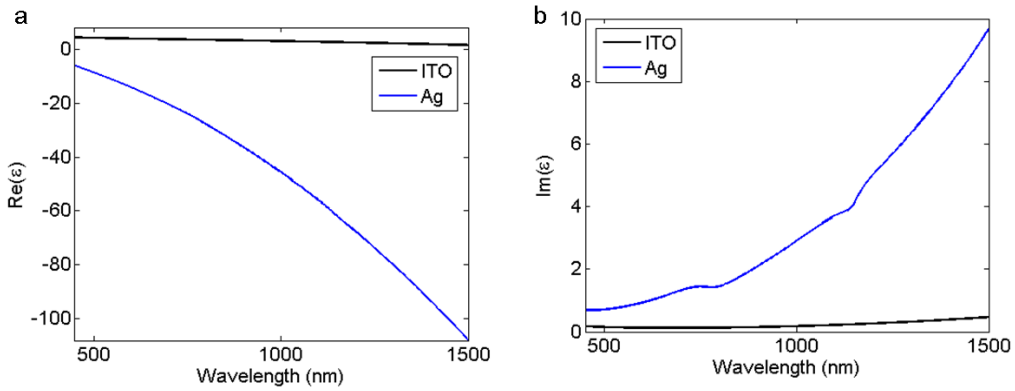

Figure S17. a) Real part of dielectric permittivity of Ag and ITO. b) Imaginary part of dielectric permittivity of Ag and ITO.

When deeply subwavelength silver inclusions are introduced into ITO host, the effective dielectric permittivity of resulting admixture can be calculated by using effective medium model in Bruggeman approximation (see Figure S18). The legend of Figure S18 indicates fill fraction of silver in ITO. Here, we extended the considered wavelength range to near-infrared. As one can see, when fill fraction of Ag in ITO varies, the dielectric permittivity of ITO/Ag mixture is modulated over broad wavelength range.

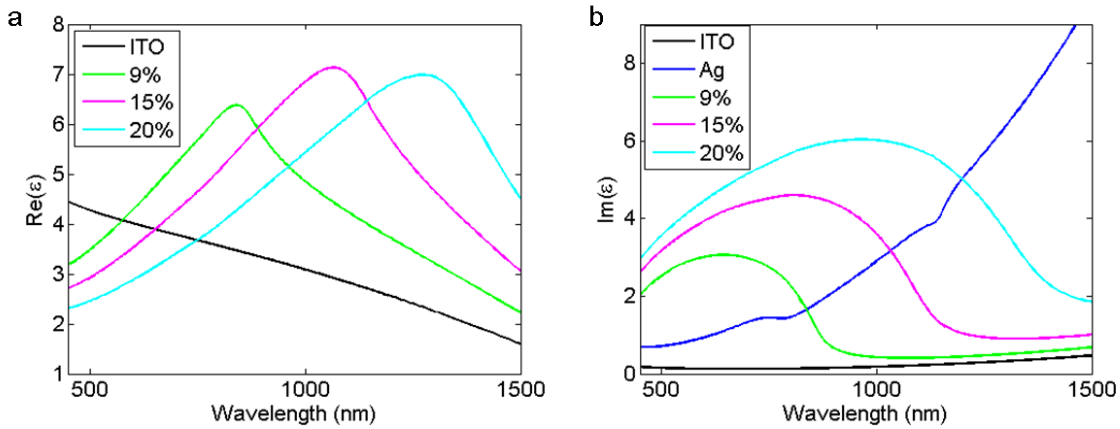

Figure S18. Effective dielectric permittivity of admixture of silver into ITO. a) plots real part of effective dielectric permittivity while b) plots corresponding imaginary part. Legends indicate fill fraction of silver into ITO. Black curves in a) and b) plot ellipsometrically measured dielectric permittivity of ITO. In b) blue curve corresponds to imaginary part of dielectric permittivity of Ag.

Since modulation mechanism proposed in our work is reminiscent to ion migration in solid state batteries, akin to the case of batteries, cyclability of our device is an important parameter to be considered. We have experimentally observed that our device shows reproducible optical behavior for at least 10^4 optical cycles.

References

[1] Y. C. Jun, J. Reno, T. Ribaudo, E. Shaner, J. J. Greffet, S. Vassant, F. Marquier, M. Sinclair, I. Brener, *Nano Lett.* **2013**, *13*, 5391; Y. W. Huang, H. W. H. Lee, R. Sokhoyan, R. A. Pala, K. Thyagarajan, S. Han, D. P. Tsai, H. A. Atwater, *Nano Lett.* **2016**, *16*, 5319; A. Olivieri, C. Chen, S. Hassan, E. Lisicka-Skrzek, R. N. Tait, P. Berini, *Nano Lett.* **2015**, 15, 2304; J. Park, J. H. Kang, X. G. Liu, M. L. Brongersma, *Sci. Rep.* **2015**, *5*, 15754.

[2] M. C. Sherrott., Philip W.C. Hon, Katherine T. Fountaine, Juan C. Garcia, Samuel M. Ponti, Victor W. Brar, Luke A. Sweatlock, H. A. Atwater, *DOI:10.1021/acs.nanolett.7b00359*; N. Dabidian, I. Kholmanov, A. B. Khanikaev, K. Tatar, S. Trendafilov, S. H. Mousavi, C. Magnuson, R. S. Ruoff, G. Shvets, *Acs Photonics* **2015**, *2*, 216.

[3] Y. Yao, M. A. Kats, P. Genevet, N. F. Yu, Y. Song, J. Kong, F. Capasso, *Nano Lett.* **2013**, *13*, 1257.

[4] J. Sautter, I. Staude, M. Decker, E. Rusak, D. N. Neshev, I. Brener, Y. S. Kivshar, *Acs Nano* **2015**, 9, 4308; O. Buchnev, N. Podoliak, M. Kaczmarek, N. I. Zheludev, V. A.

Fedotov, *Adv. Opt. Mater.* **2015**, *3*, 674; M. Decker, C. Kremers, A. Minovich, I. Staude, A. E. Miroshnichenko, D. Chigrin, D. N. Neshev, C. Jagadish, Y. S. Kivshar, *Opt. Express* **2013**, *21*, 8879.
[5] M. J. Dicken, K. Aydin, I. M. Pryce, L. A. Sweatlock, E. M. Boyd, S. Walavalkar, J. Ma, H. A. Atwater, *Opt. Express* **2009**, *17*, 18330.
[6] Y. G. Chen, T. S. Kao, B. Ng, X. Li, X. G. Luo, B. Luk'yanchuk, S. A. Maier, M. H. Hong, *Opt. Express* **2013**, *21*, 13691; B. Gholipour, J. F. Zhang, K. F. MacDonald, D. W. Hewak, N. I. Zheludev, *Adv. Mater.* **2013**, *25*, 3050.
[7] E. D. Palik, G. Ghosh, *Handbook of optical constants of solids*, Academic Press, San Diego **1998**.